Energy & Environmental Science

ROYAL SOCIETY OF CHEMISTRY

PAPER

View Article Online
View Journal | View Issue

Cite this: *Energy Environ. Sci.*, 2025, **18**, 1375

Manipulating crystallization kinetics and vertical phase distribution *via* a small molecule donor guest for organic photovoltaic cells with 20% efficiency†

Bo Cheng,[a] Wenwen Hou,[a] Chenyu Han,[a] Sixuan Cheng,[a] Xinxin Xia,[a] Xia Guo, *[a] Yongfang Li [b] and Maojie Zhang *[ab]

Received 8th October 2024,
Accepted 9th December 2024

DOI: 10.1039/d4ee04623d

rsc.li/ees

Precise control over molecular crystallization and vertical phase distribution of photovoltaic bulk-heterojunction (BHJ) films is crucial for enhancing their optoelectronic properties toward high-performance polymer solar cells (PSCs). Herein, a kinetics-controlling strategy is implemented in the PM6:L8-BO blend system by introducing a small molecule donor (SMD), namely BTR-SCl, which possesses strong crystallization properties and excellent miscibility with the host polymer donor. *In situ* spectroscopic characterization indicates that BTR-SCl can effectively advance the aggregation of PM6 from the blend solution and prolong its self-assembly time during the film formation process, which leads to well-defined vertical phase distribution with a more ordered polymer donor enriched at the anode, effectively facilitating charge transport and collection, alleviating trap density and energetic disorder, and reducing energy loss. Ultimately, the PM6:BTR-SCl:L8-BO ternary PSCs (T-PSCs) achieve a remarkably enhanced power conversion efficiency (PCE) of 19.4% in comparison with 18.0% for the binary device. Notably, by replacing PM6 with D18, the PCE of ternary devices is further boosted to 20.0%, which represents the highest efficiency for SMD-based T-PSCs reported to date. Our findings elucidate the great potential of crystalline SMD in optimizing the vertical phase distribution and molecular packing within the BHJ film, leading to considerable improvements in the PCE of PSCs.

Broader context

Bulk-heterojunction (BHJ) polymer solar cells (PSCs) have emerged as a promising energy conversion technology, attracting considerable attention due to their advantageous characteristics of light weight, flexibility, and easy fabrication. Though promising, the precise control of morphology in the BHJ active layer remains a significant challenge, owing to the intricate relationship between material crystallization and phase separation. In this study, we have proposed a feasible kinetics-controlling strategy to modulate the assembly behavior of the host polymer donor by introducing a small molecule donor guest, BTR-SCl. The strong crystallization properties of BTR-SCl, in conjunction with its excellent miscibility with the host polymer donor, markedly accelerated the aggregation of the polymer donor from the blend solution and extended its self-assembly time during the film formation process. This facilitated favorable vertical phase distribution and reinforced ordered molecular stacking within BHJ films. Ultimately, our strategy achieved an impressive power conversion efficiency of 20.0% in the D18:BTR-SCl:L8-BO system. This work not only deepens our understanding of the factors influencing morphology control but also offers a rational framework for the modulation of multi-component techniques.

1. Introduction

Polymer solar cells (PSCs) are regarded as essential technologies for future energy demands, due to their solution processability, lightweight nature, and high mechanical durability.[1–3] Despite the remarkable progress of PSCs in the past few years, with single-junction PSCs having achieved power conversion efficiencies (PCEs) exceeding 20%, their performance continues to be impeded by sub-optimal carrier generation, transport,

[a] *National Engineering Research Center for Colloidal Materials, Key Laboratory of Special Functional Aggregated Materials (Shandong University), Ministry of Education, School of Chemistry & Chemical Engineering, Shandong University, Jinan, Shandong 250100, China. E-mail: mjzhang@sdu.edu.cn, guoxia0610@sdu.edu.cn*

[b] *Suzhou Key Laboratory of Novel Semiconductor-optoelectronics Materials and Devices, College of Chemistry, Suzhou Key Laboratory of Novel Semiconductor-optoelectronics Materials and Devices, College of Chemistry Chemical Engineering and Materials Science, Soochow University, Suzhou 215123, China*

† Electronic supplementary information (ESI) available. See DOI: https://doi.org/10.1039/d4ee04623d

and collection processes.[4–8] In contrast to highly crystallized inorganic and hybrid semiconductors like silicon and perovskite, organic semiconductors typically exhibit a disordered structure, leading to poor carrier transport mobility and severe bimolecular recombination in PSCs.[9–14] Consequently, state-of-the-art PSCs merely reach fill factors (FFs) of roughly 80%, lower than those of their inorganic counterparts where FFs exceeding 87% have been achieved.[15–17] The construction of ordered molecular configurations within PSCs has been sought toward decreasing FF losses to realize record-breaking PCEs.[18–21]

Apart from the above-mentioned disordered nature of organic semiconductors, PSCs operate as excitonic photovoltaics and generally need the existence of both electron donor and electron acceptor materials within the active layer to establish a bulk heterojunction (BHJ).[22] During film formation, the intricate interplay of three phases, influenced by the varying crystallization and thermodynamic properties of photovoltaic materials, complicates efforts to control morphology.[23–26] Thus, optimizing the BHJ morphological properties, such as crystallization, domain size, and vertical phase distribution, to boost the efficiency and stability of PSCs is still a dominant hotspot in the community.[27–29]

A versatile approach to manipulating the BHJ morphology involves introducing a guest component capable of preferentially interacting with a host donor or acceptor, thereby fostering favorable morphology evolution.[30–32] Since the advent of diverse non-fullerene acceptors (NFAs), extensive research has been focused on incorporating a guest, either a polymer donor or NFA, into the photoactive layer, which is more highly compatible with the existing donors or acceptors.[33–36] Nonetheless, reports on efficient ternary PSCs (T-PSCs) using small molecule donors (SMDs) as the third component are relatively scarce. Given that SMDs typically possess high crystallinity and inherent advantages such as a precise chemical structure, low energy disorder, and minimal batch-to-batch variation compared to polymers, SMDs should be a powerful candidate for constructing effective T-PSCs.[37,38]

In our previous studies, we incorporated a highly crystalline SMD BTTzR into the binary PM6:Y6 PSCs.[39] The favorable miscibility between BTTzR and Y6 successfully mitigated the over-aggregation of Y6, leading to a notably low nonradiative voltage loss of 0.19 eV in BHJ and, thus, an increment in the PCE of PSCs. Not long ago, Xiao *et al.* developed a highly crystalline SMD, BTTC, by incorporating the rigid thieno[3,2-*b*]thiophene substituent unit.[40] BTTC could migrate into the donor phase in the PM6:L8-BO-based T-PSCs, synergistically optimizing the crystallinity and vertical phase separation in BHJ. As a result, an impressive PCE of 18.8% was achieved in the PM6:BTTC:L8-BO system. Likewise, Li's group incorporated a novel conjugated molecule SD-EDOT with multiple conformation locks into the PM6:L8-BO blend to construct T-PSCs. The PM6:SD-EDOT:L8-BO device demonstrated enhanced charge transport mobility and achieved an excellent PCE of 19.3%.[41] The above works clearly demonstrate that integrating crystalline SMDs into the binary PSCs is conducive to modulating the BHJ morphology. However, such refined crystallinity and/or phase separation achieved through SMD-assisted ternary strategies remains merely a phenomenon, which falls short of explaining mechanisms and achieving higher performance. Elucidating the intrinsic morphology evolution process within the BHJ, especially from the viewpoint of regulating the aggregation characteristics of the host donor or acceptor, is crucial for understanding the pivotal role of SMDs in T-PSCs, yet little information is available in this regard.

In this work, we constructed highly efficient T-PSCs by incorporating a SMD, named BTR-SCl, into the PM6:L8-BO host matrix, striving to elucidate the intrinsic morphological evolution mechanism in the ternary system. In our previous work,[42] it has been reported that BTR-SCl exhibited strong crystallization property and good miscibility with the polymer as well as complementary absorption and cascade energy level with the host active layer, showing great potential for application in T-PSCs. *In situ* and *ex situ* morphological characterization studies disclosed that the strong crystallinity and compatibility of BTR-SCl enable earlier aggregation of PM6 with slower crystallization kinetics during the film formation process, which offers a pronounced vertical phase distribution with enhanced molecular ordering in the bulk phase. The charge carrier dynamics and energy loss results underscored that the enhanced charge transport and diminished trap density and energetic disorder simultaneously contributed to the improved open-circuit voltage (V_{OC}). Benefiting from these advantages, the T-PSC with 10 wt% BTR-SCl obtained an impressive PCE of 19.4% with an excellent FF of 81.5%, significantly outperforming those of PM6:L8-BO-based binary PSCs. Meanwhile, the ternary devices also demonstrated obviously extended photostability and thermal stability. Furthermore, upon replacing PM6 with D18, an inspiring PCE of 20.0% was recorded in the D18:BTR-SCl:L8-BO ternary blend system, which stands for the highest efficiency for SMD-based T-PSCs reported so far. Therefore, this work elucidates the delicate morphology-tuning effect of SMDs in improving the device performances of PSCs.

2. Results and discussion

2.1. Optical and electrochemical properties

The molecular structures and the energy levels diagrams of PM6, BTR-SCl, and L8-BO are depicted in Fig. 1a and b. It can be seen that the cascade energy alignment among the three materials is formed, which can help mitigate the charge transfer barrier and facilitate charge separation.[43] Besides, the relatively lower highest occupied molecular orbital (HOMO) energy level of BTR-SCl (−5.51 eV) compared to that of PM6 (−5.40 eV) suggests potential advantages for attaining higher V_{OC} in a ternary system. The normalized ultraviolet-visible–near-infrared (UV-vis-NIR) absorption spectra of the host PM6 and L8-BO films are overlaid in Fig. 1c, which coordinates appropriately with that of the SMD BTR-SCl. The maximum absorption peak of BTR-SCl lies at 641 nm, and its predominant absorption range spans from 521 to 700 nm, forming

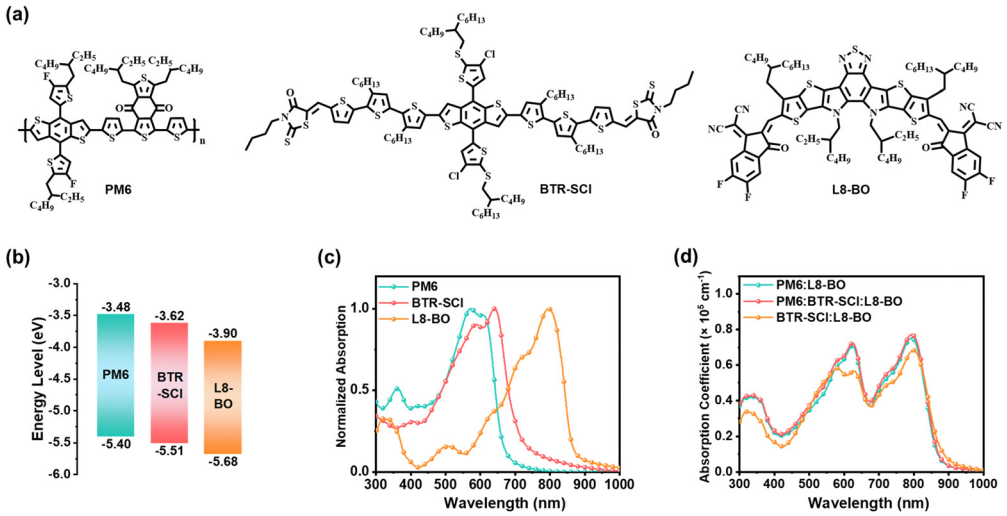

Fig. 1 (a) Molecular structures, (b) energy levels, and (c) film absorption spectra of PM6, BTR-SCl, and L8-BO, (d) absorption coefficients of PM6:L8-BO, PM6:BTR-SCl:L8-BO, and BTR-SCl:L8-BO blend films.

complementary absorption spectra and allowing for substantial photon harvesting with host PM6 (absorption peak at 573 nm) and L8-BO (absorption peak at 796 nm). The absorption changes of neat films with and without BTR-SCl were investigated. As exhibited in Fig. S1a (ESI†), compared with the PM6 film, upon adding BTR-SCl into PM6, the blend film exhibits a pronounced red-shift absorption with an enhanced (0–0) absorption peak. In contrast, the absorption profile of the L8-BO film exhibits negligible changes when BTR-SCl is added (Fig. S1b, ESI†). These results suggest that the influence of BTR-SCl on PM6 is much greater than that on L8-BO in terms of molecular ordered stacking.[44] We further measured the absorption coefficients for different binary and ternary active layers (Fig. 1d). It can be seen that the PM6 : BTR-SCl : L8-BO (0.9 : 0.1 : 1.2) film presents a higher absorption coefficient both in the PM6 and L8-BO absorption region than in the binary film, which demonstrates its stronger capability for light harvesting and potentially leads to a larger short-circuit current density (J_{SC}) in actual T-PSCs.

2.2. Photovoltaic properties

PSCs featuring a traditional configuration of indium tin oxide (ITO)/poly(3,4-ethylenedioxythiophene)poly(styrenesulfonate): (PEDOT:PSS)/active layer/poly[[2,7-bis(2-ethylhexyl)-1,2,3,6,7,8-hexahydro-1,3,6,8-tetraoxobenzo[lmn][3,8]phenanthroline-4,9-diyl]-2,5-thiophenediyl[9,9-bis[3-(dimethylamino)propyl]-9*H*-flu-orene-2,7-diyl]-2,5-thiophenediyl](PNDIT-F3N)/Ag were prepared to investigate the impact of the BTR-SCl guest on the photovoltaic characteristics of the device. We conducted a detailed optimization of solar cells by varying the incorporated content of the guest component to obtain the optimal performance (Fig. S2 and Table S1, ESI†). The optimized current density–voltage (J–V) characteristics are depicted in Fig. 2a and their corresponding photovoltaic parameters are presented in Table 1. The referential PSCs based on PM6 : L8-BO (1 : 1.2) blends provided PCE of 18.0%, with V_{OC} of 0.88 V, J_{SC} of 26.2 mA cm^{-2}, and FF of 78.1%, being comparable to the reported values.[35] For the BTR-SCl:L8-BO devices, a poor PCE of 9.9% with high V_{OC} of 0.90 V, low J_{SC} of 17.7 mA cm^{-2}, and FF of 61.7% was observed. Particularly, after adding 10 wt% loading of BTR-SCl into PM6:L8-BO blends, the PM6 : BTR-SCl : L8-BO (0.9 : 0.1 : 1.2) ternary device exhibited a remarkable PCE of 19.4%, owing to the simultaneous increase in V_{OC} (0.89 V), J_{SC} (26.8 mA cm^{-2}) and FF (81.5%), compared with the PM6:L8-BO PSCs. It is worth noting that the FF and PCE are also among the highest values in reported SMD-based T-PSCs (Fig. 2b and Table S2, ESI†). Inspired by the impressive photovoltaic performance of BTR-SCl, we additionally introduced BTR-SCl into the binary systems based on D18:L8-BO and evaluated its applicability (Fig. S3a, ESI†). Encouragingly, akin to the performance in the PM6:L8-BO system, improvements in V_{OC}, J_{SC}, and FF were noted, delivering an outstanding PCE of 20.0% (Table 1 and Fig. S3b, ESI†). To the best of our knowledge, 20% PCE represents the highest efficiency for SMD-based T-PSCs reported to date (Fig. 2b). The J_{SC} values of the solar cells are also validated by the external quantum efficiency (EQE) spectra (Fig. 2c and Fig. S3c, ESI†), in which the calculated current densities align well with the trends attained from the J–V measurements. The effect of BTR-SCl on the device stability was further evaluated. As shown in Fig. 2d, the PM6:BTR-SCl:L8-BO T-PSC display improved photostability. Specifically, the BTR-SCl-based ternary device maintains 80% of the initial efficiency after 135 hours of constant illumination under a 100 mW cm^{-2} LED, while the PCE of the binary device decays to 72%. We also studied the thermal stability of these devices. As presented in Fig. S4 (ESI†), the PCE of the binary PSC rapidly drops to 60% of its original value upon constant heating at 85 °C for 213 hours in an N_2-filled glove box, whereas the BTR-SCl-based T-PSC retains 70% of the initial PCE, indicating ameliorated thermal stability in ternary solar cells.

2.3. Charge carrier dynamics

To explore the variations in opto-electrical behaviors among these devices, the carrier dynamics, including exciton dissociation,

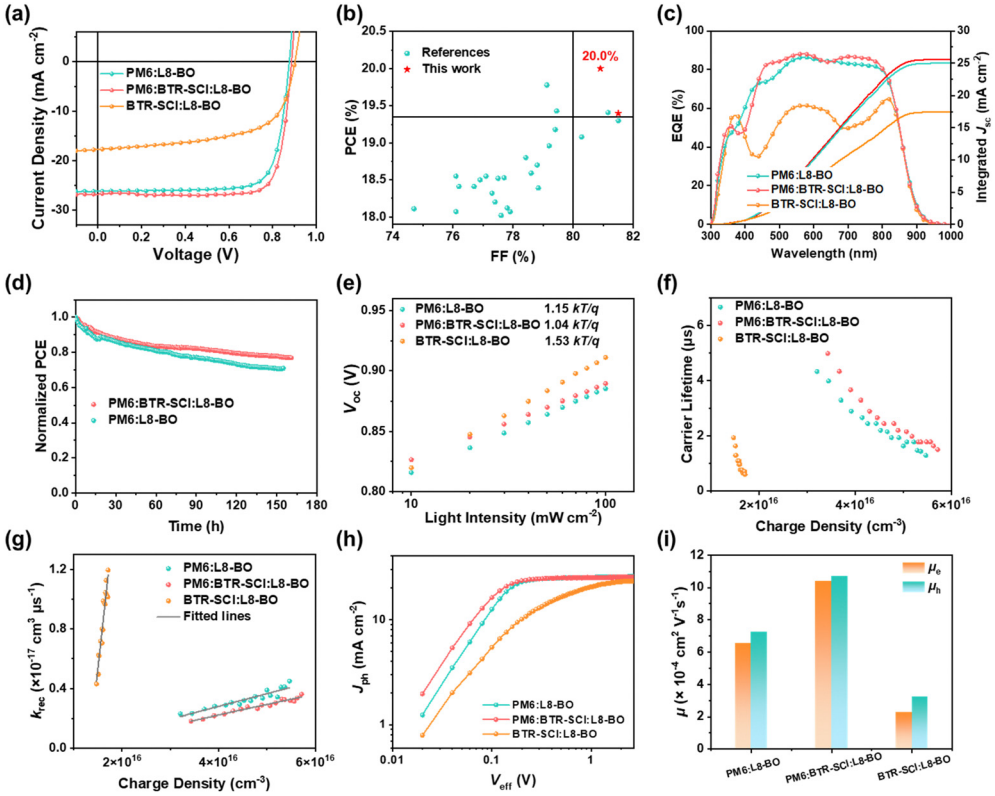

Fig. 2 (a) J–V curves of three PSCs. (b) PCEs *vs.* fill factor (FF) in SMD-based T-PSCs (PCE ≥ 18%). (c) EQE spectra of three PSCs. (d) Photostability of unencapsulated PM6:L8-BO and PM6:BTR-SCl:L8-BO PSCs in the glovebox under one sun illumination. (e) V_{OC} as functions of light intensity for the three PSCs. (f) Carrier lifetime *versus* charge density for the three PSCs. (g) Bimolecular charge recombination rates (k_{rec}) *versus* charge density for the three PSCs. (h) J_{ph} *versus* V_{eff} curves of three PSCs. (i) The hole and electron mobilities of three PSCs.

Table 1 Photovoltaic performance of the binary and ternary PSCs

Active layer	V_{OC} (V)	J_{SC}/J_{cal}[a] (mA cm^{-2})	FF (%)	PCE[b] (%)
PM6:L8-BO	0.88	26.2/25.0	78.1	18.0 (17.8 ± 0.2)
PM6:BTR-SCl:L8-BO	0.89	26.8/25.6	81.5	19.4 (19.1 ± 0.2)
BTR-SCl:L8-BO	0.90	17.7/17.4	61.7	9.9 (9.6 ± 0.3)
D18:L8-BO	0.91	26.3/25.2	79.3	18.9 (18.8± 0.1)
D18:BTR-SCl:L8-BO	0.92	26.9/25.8	80.9	20.0 (19.8± 0.2)

[a] The integrated current densities from the EQE curves. [b] The statistical values in parentheses were averaged from 10 cells.

carrier transport, and recombination, were investigated. We examined the relationship of J_{SC} and V_{OC} with irradiation intensity (P_{light}) to explore the charge recombination in both binary and ternary PSCs. As shown in Fig. 2e, the slopes of V_{OC} *versus* P_{light} were fitted to be 1.15, 1.04, and 1.53 kT/q for PM6:L8-BO, PM6:BTR-SCl:L8-BO, and BTR-SCl:L8-BO devices, respectively. Besides, by fitting the J_{SC}–P_{light} curves using the formula $J_{SC} \propto P_{light}^{\alpha}$, where α is used to evaluate the bimolecular recombination of devices, the α values for the PM6:L8-BO, PM6:BTR-SCl:L8-BO, and BTR-SCl:L8-BO devices were calculated to be 0.98, 0.99, and 0.92, respectively (Fig. S5, ESI†). Notably, the smallest slope of 1.04 kT/q and the largest α of 0.99 for the PM6:BTR-SCl:L8-BO ternary device indicate significant suppression of both bimolecular and trap-assisted recombination, consequently contributing to enhanced J_{SC} and FF values. Furthermore, we employed the transient photovoltage (TPV) and charge extraction (CE) measurements to evaluate the carrier recombination kinetics in the three PSCs. As shown in Fig. 2f, the PM6:BTR-SCl:L8-BO ternary device exhibits a higher carrier density (n) and longer carrier lifetime than the binary devices. Moreover, the bimolecular charge recombination rates (k_{rec}) of the PSCs can be further quantified as a function of n (Fig. 2g).[45] Compared to the binary PSCs, the k_{rec} values of the ternary device are still lower across various n values, further proving its lowest recombination loss in the PM6:BTR-SCl:L8-BO device.

The exciton dissociation (P_{diss}) and charge collection (P_{coll}) efficiencies were studied by examining the dependence of photocurrent (J_{ph}) on effective voltage (V_{eff}) curves (Fig. 2h). As listed in Table S3 (ESI†), the highest P_{diss} and P_{coll} values of 99.8% and 93.6%, respectively, for the PM6:BTR-SCl:L8-BO PSC manifest its admirable capability of exciton dissociation and carrier generation. The photoluminescence (PL) measurements of the neat films and blend films in Fig. S6 (ESI†) show that the PM6:BTR-SCl:L8-BO blends present the highest PL quenching efficiency of over 97%, further corroborating that more exciton dissociation occurring in T-PSCs.[46] Meanwhile, transient photocurrent measurements (TPC) (Fig. S7, ESI†) demonstrate that PM6:BTR-SCl:L8-BO device yields the shortest photocurrent decay time of 0.15 μs than those of PM6:L8-BO (0.29 μs)

and BTR-SCl:L8-BO (0.50 μs) counterparts, signifying the enhanced charge extraction efficiency of ternary devices. The carrier transport capability in active layers was further studied *via* leveraging space-charge-limited current (SCLC) measurements (Fig. 2i, Fig. S8 and Table S4, ESI†). Regarding the PM6:L8-BO devices, the incorporation of BTR-SCl led to an augmentation in both hole mobility (μ_h) and electron mobility (μ_e) within the PM6:BTR-SCl:L8-BO PSC, with the μ_h and μ_e increasing from 7.26×10^{-4} to 1.07×10^{-3} V^{-1} s^{-1}, and from 6.54×10^{-4} to 1.04×10^{-3} V^{-1} s^{-1}, respectively. Apparently, the highest carrier mobilities and perfectly balanced carrier transport (μ_h/μ_e of 1.03) are achieved in the optimal PM6:BTR-SCl:L8-BO device, which is consistent with their FF enhancement. These results clearly demonstrate the capability of BTR-SCl as the guest donor to simultaneously facilitate the exciton dissociation and carrier generation, thereby comprehensively benefiting the J_{SC} and FF of the device.

2.4. Energy loss

To discover the enhanced V_{OC} in the PM6:BTR-SCl:L8-BO system, we analyzed energy losses (E_{loss}) in both cells by measuring their external electroluminescence quantum efficiency (EQE_{EL}) and highly sensitive external quantum efficiency (sEQE) spectra. The total E_{loss} in PSCs can be separated into three parts; the detailed calculation method is provided in ESI,† with relevant results summarized in Table S5 (ESI†).[47] As depicted in Fig. 3a and b, the bandgaps (E_g) of PM6:L8-BO and PM6:BTR-SCl:L8-BO, derived from electroluminescence (EL) and sEQE spectra of the two cells, are 1.441 and 1.446 eV respectively. Therefore, their total E_{loss} ($E_{loss} = E_g - V_{OC}$) are estimated to be 0.561 and 0.556 eV. These values indicate that BTR-SCl effectively reduces E_{loss} in PM6:L8-BO PSCs. The EQE_{EL} was also measured as shown in Fig. 3c, which is 9.40×10^{-5} for PM6:L8-BO and 1.40×10^{-4} for PM6:BTR-SCl:L8-BO. It is observed that the PM6:BTR-SCl:L8-BO-based device exhibits a higher EQE_{EL} than the PM6:L8-BO ones, suggesting smaller nonradiative E_{loss} (ΔE_3) of 0.230 eV compared to 0.240 eV of the PM6:L8-BO-based device. To further explore the origin of lower ΔE_3 in PM6:BTR-SCl:L8-BO-based PSCs, exponential fittings of sub-bandgaps of the sEQE spectra were conducted based on the Urbach rule (Fig. 3d).[48] It is revealed that the PM6:BTR-SCl:L8-BO PSC shows a lower Urbach energy (E_U) of 22.2 meV compared to the PM6:L8-BO-based PSC (22.8 meV), indicating reduced energetic disorder in the PM6:BTR-SCl:L8-BO matrix.[49] In addition, the trap density of the PSCs was further quantified from the capacitance-frequency characteristics (Fig. S9, ESI†).[50,51] As shown in Fig. 3e, the PM6:L8-BO film possesses a higher total state density (N_t) value of 1.12×10^{16} cm^{-3}. In contrast, with the assistance of BTR-SCl, the PM6:BTR-SCl:L8-BO film exhibits a suppressed N_t value of 0.94×10^{16} cm^{-3}. Overall, the ordered molecular packing (which will be discussed later) and cascaded energy level alignments in PM6:BTR-SCl:L8-BO film, induced by the integration of the SMD BTR-SCl, should be responsible for its restrained energetic disorder and trap density and, thus, mitigated recombination loss of the relevant PSCs.[52]

2.5. Film morphology

The compatibility of BTR-SCl with the host components performs a crucial role in determining the spatial distribution of BTR-SCl within the photoactive layer. Consequently, differential scanning calorimetry (DSC) was employed to investigate the alterations in melting behavior of BTR-SCl and its binary blends. As depicted in Fig. S10 (ESI†), while PM6 shows no distinct melting peak during the heating process, BTR-SCl presents two endothermic peaks at 245 °C and 261 °C respectively. The melting peaks of BTR-SCl disappear after being mixed with PM6 (PM6 : BTR-SCl, w/w = 0.9 : 0.1), which implies a high degree of miscibility between BTR-SCl and PM6 in this instance. In contrast, upon blending with BTR-SCl

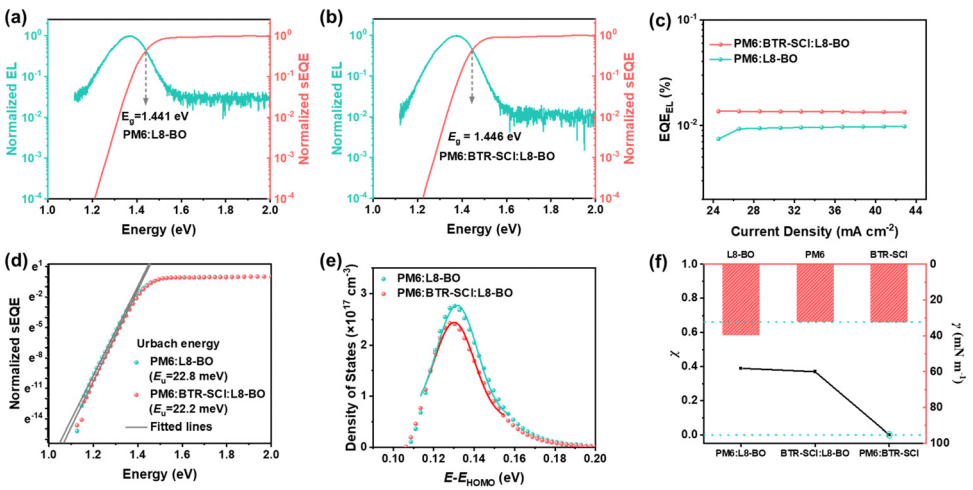

Fig. 3 The derived bandgaps in (a) PM6:L8-BO- and (b) PM6:BTR-SCl:L8-BO-based PSCs. (c) EQE_{EL} curves of PM6:L8-BO- and PM6:BTR-SCl:L8-BO-based PSCs. (d) sEQE curves of PM6:L8-BO- and PM6:BTR-SCl:L8-BO-based PSCs and their Urbach energy (E_u) values. (e) Density of states curves of PM6:L8-BO- and PM6:BTR-SCl:L8-BO-based PSCs. (f) Surface energy (γ) of PM6, BTR-SCl, and L8-BO film and the Flory–Huggins interaction parameter (χ) of the PM6:BTR-SCl, PM6:L8-BO, and BTR-SCl:L8-BO blend films.

(w/w = 1.1 : 0.1), the melting point of L8-BO decreases from 322 °C to 315 °C. Moreover, a new melting point at 254 °C appears, indicating that the BTR-SCl and L8-BO are hardly compatible in the blends. Besides, the contact angle test was also conducted to verify the compatibility of BTR-SCl with PM6 and L8-BO. As shown in Fig. 3f, Fig. S11, and Table S6 (ESI†), the surface energy of PM6, BTR-SCl, and L8-BO films turn out to be 32.05, 32.28, and 39.53 mN m^{-1}, respectively. Similarly, the Flory–Huggins interaction parameter (χ) between the two materials can be calculated based on their surface energies to assess their miscibility, and the calculation method is detailed in the ESI.† The χ value between PM6 and BTR-SCl came out to be 0.0004 κ, much smaller than 0.37 κ of BTR-SCl:L8-BO and 0.39 κ of PM6:L8-BO films. Such a low χ value of PM6:BTR-SCl indicates that they are more inclined to form an "alloy-like" donor phase, which is consistent with the DSC results.[53] We further conducted grazing-incidence wide-angle X-ray scattering (GIWAXS) experiments to investigate the packing behavior of molecules in both neat and blend films (Fig. 4 and Fig. S12, ESI†), and the scattering parameters were summarized in Table S7 (ESI†). Both PM6 and L8-BO films show a typical "face-on" molecular arrangement, with scattering peaks from lamellar stacking appearing along the in-plane (IP) direction and π–π stacking peaks along the out-of-plane (OOP) direction. In contrast, the BTR-SCl neat film displays distinctive lamellar and π–π stacking peaks in both IP and OOP directions, suggesting the coexistence of "face-on" and "edge-on" orientation. The crystal correlation length (CCL) of the three neat materials was calculated using the Scherrer equation. It can be observed that the BTR-SCl film exhibits a larger CCL of 27.40/127.94 Å along the OOP/IP, much larger than that of PM6 (20.59/81.54 Å) and L8-BO (14.52/88.70 Å) films. The noticeably increased CCLs suggest that BTR-SCl has extremely high crystallinity. Compared with the PM6 neat film, after adding 10 wt% BTR-SCl, larger CCLs are also observed along both OOP and IP axes for PM6:BTR-SCl films with the CCL values increased to 21.45 and 84.39 Å respectively. Meanwhile, smaller *d*-spacing values both for lamellar stacking and π–π stacking are also found in the PM6:BTR-SCl system. Shorter intermolecular packing distances along with larger CCLs confirm that BTR-SCl can effectively improve the structural order of PM6. Likewise, for PM6:L8-BO, PM6:BTR-SCl:L8-BO and BTR-SCl:L8-BO blends, their π–π stacking peaks in the OOP direction lie at 1.82 Å, 1.83 Å, and 1.77 Å, respectively, corresponding to *d*-spacings of 3.45 Å, 3.43 Å and 3.55 Å. Furthermore, the calculated CCL values for π–π stacking peaks of PM6:L8-BO, PM6:BTR-SCl:L8-BO, and BTR-SCl:L8-BO are 21.57 Å, 22.15 Å, and 14.82 Å, respectively. These findings can be ascribed to the strong interactions between PM6 and the highly crystalline BTR-SCl, which create a new hybrid phase with closer molecular stacking and enhanced crystallization of polymer PM6 in the ternary system. Ternary films with this kind of bulk

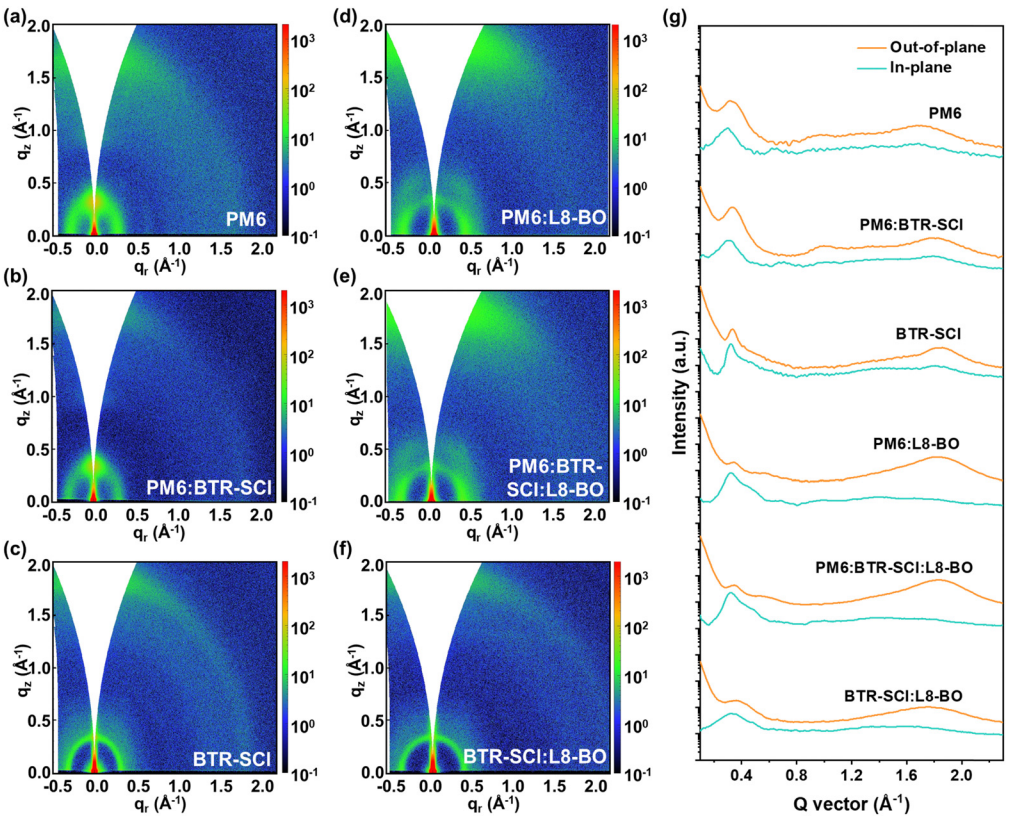

Fig. 4 GIWAXS patterns of (a) PM6, (b) PM6:BTR-SCl, (c) BTR-SCl, (d) PM6:L8-BO, (e) PM6:BTR-SCl:L8-BO, and (f) BTR-SCl:L8-BO films. (g) Corresponding 1D line-cuts profiles.

morphology would provide an ideal channel for exciton dissociation and carrier transport.

Furthermore, atomic force microscopy (AFM) and transmission electron microscopy (TEM) (Fig. S13, ESI†) were employed to understand the effect of BTR-SCl on the surface and bulk morphology of the blends. PM6:L8-BO, PM6:BTR-SCl:L8-BO and BTR-SCl:L8-BO blends exhibit smooth surfaces with small root-mean-square roughness (R_q) values of 1.02, 1.07, and 1.55 nm, respectively. Compared to the control PM6:L8-BO binary films, upon integrating with the highly crystalline SMD BTR-SCl, slightly enhanced phase separation and larger grain-like aggregates in ternary blends are detected in the AFM phase image and TEM images, which are desirable for enhancing carrier transport and collection in ternary cells.

As is well known, vertical distribution of components within the photoactive BHJ is of great significance for the carrier transport and collection in PSCs.[54] Hence, we carried out film depth-dependent light absorption spectroscopy (FLAS) to explore the effect of BTR-SCl on vertical phase separation within the PM6:L8-BO blends. As plotted in Fig. 5a and b, PM6 and L8-BO exhibit absorption peaks at 623 and 796 nm, respectively. Apparently, in comparison with the PM6:L8-BO, the absorption peaks of PM6 and L8-BO in ternary PM6:BTR-SCl:L8-BO are more consistent along the film-depth direction, suggesting a more homogeneous distribution of energy levels in ternary films, which should contribute to its smaller energetic disorder within the active layer.[55] Upon fitting the FLAS plots with the absorption spectra of neat PM6 and L8-BO films, the composition distribution profiles can be deduced. Fig. 5c underscores a prevalent distribution of the L8-BO at the bottom-half region in PM6:L8-BO, potentially hindering charge collection. In contrast, adding BTR-SCl results in synergistically improved acceptor content in the upper half of the films, as well as donor enrichment layer near the anode (Fig. 5d). Such a distinctive phase distribution structure along vertical direction is advantageous for efficient carrier transport and extraction.

To understand the influence of BTR-SCl on BHJ formation kinetics, the emerging *in situ* UV-vis absorption technology was utilized to capture the aggregation process of PM6 and L8-BO during film formation evolving from the liquid to the solid state. Fig. 5e, f and Fig. S14 (ESI†) present the representative absorption spectra of the PM6:L8-BO and PM6:BTR-SCl:L8-BO blends during the film formation process. The evolution of peak positions was extracted from the raw absorption spectra and employed to investigate the aggregation kinetics of the host components. As shown in Fig. 5g and h, the entire film formation process can be separated into stages I–III, namely solvent-evaporation (stage I), nucleation and crystal-growth (stage II), and film-drying (stage III). In stage I, the peak positions of PM6 and L8-BO in both binary and ternary films do not change obviously. As the solvent slowly evaporates (stage II), the solution concentration reaches supersaturation, and then the solute molecules begin to nucleate. Under such oversaturated conditions, the absorption peaks of both components appear to undergo red-shift, indicating the onsets of their crystallization process.[56] The red-shifting of PM6 absorption peak in PM6:BTR-SCl:L8-BO (t = 0.35 s) is much earlier than the L8-BO absorption peak (t = 0.39 s), suggesting the earlier aggregation of PM6 compared to L8-BO. For the binary counterpart, in contrast, the red-shifting onset of the PM6 absorption peak (0.40 s) lags behind that of L8-BO (0.34 s). Therefore, the incorporation of BTR-SCl into the PM6:L8-BO blends can effectively advance the aggregation of PM6. Moreover, upon adding BTR-SCl, the time scale of stage II during PM6 self-assembly increased greatly from 0.09 s to 0.17 s, while only a slightly prolonged time is observed for L8-BO (from 0.15 s to 0.16 s). The earlier molecular aggregation and elongated crystallization time of PM6 in PM6:BTR-SCl:L8-BO may facilitate its compact and ordered packing and formation of the favorable vertical phase distribution, which is consistent with the GIWAXS and FLAS results above.[29]

Taking into account all the discussions above, a schematic diagram illustrating how BTR-SCl induces the vertical phase

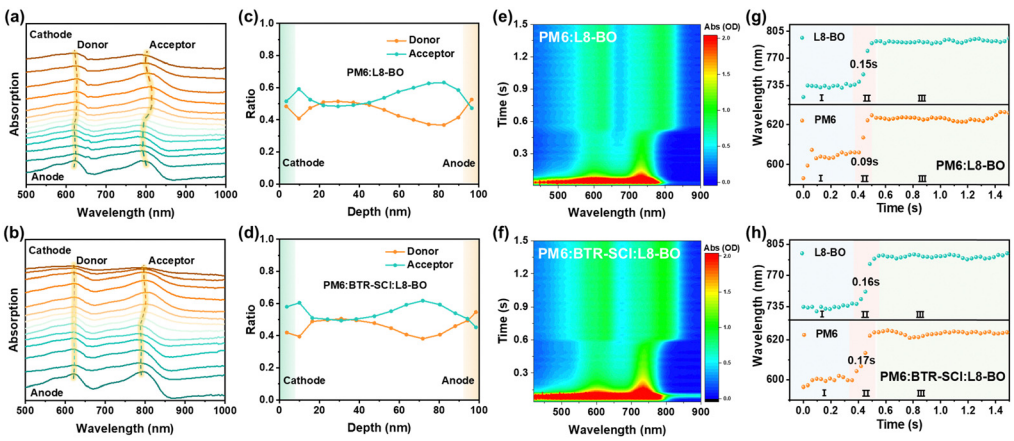

Fig. 5 FLAS absorption spectra for (a) PM6:L8-BO and (b) PM6:BTR-SCl:L8-BO films. Composition distribution profiles as a function of film depth for (c) PM6:L8-BO and (d) PM6:BTR-SCl:L8-BO films. (e) and (f) *In situ* 2D UV-vis absorption mapping of PM6:L8-BO and PM6:BTR-SCl:L8-BO active layers during spin coating. (g) and (h) Time evolution of the PM6 and L8-BO peak positions extracted from the absorption contour in PM6:L8-BO and PM6:BTR-SCl:L8-BO active layers during spin coating.

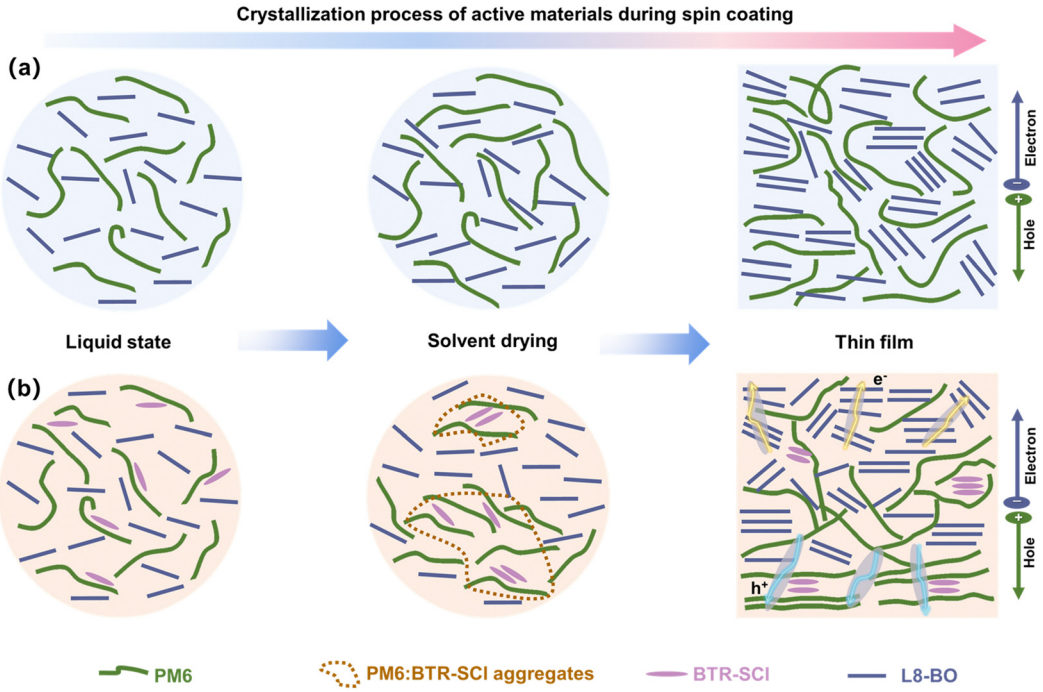

Fig. 6 Schematic illustration of the crystallization process for (a) PM6:L8-BO and (b) PM6:BTR-SCl:L8-BO BHJ during film formation.

configuration and enhances the crystallinity of the photoactive layer is presented in Fig. 6. In the solution stage, BTR-SCl tends to mix with PM6 due to their excellent miscibility. Benefiting from its strong aggregation properties, BTR-SCl can effectively promote the pre-aggregation of PM6 during the film formation process, leading to the aggregation of PM6 occurring earlier than that of L8-BO. The earlier molecular aggregation may result in PM6 precipitating out earlier in the bottom region, thus creating an acceptor-rich assembly near the cathode. This distinctive morphological evolution ultimately facilitates the establishment of a classic D/D:A/A configuration within the BHJ film. In addition, the prolonged molecular crystallization time could also enable PM6 to assemble more sufficiently, promoting more compact and ordered molecular stacking. Accordingly, vertical phase morphology with desired material distribution and better molecular ordering of PM6 is achieved.

3. Conclusions

We put forward a simple and effective kinetics-controlling strategy to enable refined molecular crystallization and vertical phase distribution towards high-performance T-PSCs. The detailed film formation kinetics were probed and their direct connections with BHJ morphology were revealed for both ternary and binary films, *via* combined *in situ* spectroscopy and *ex situ* morphological analysis. It was found that, due to the strong crystallization properties of BTR-SCl and its good compatibility with the host polymer donor, the BTR-SCl guest can advance the aggregation of the polymer donor PM6 from blend solution and elongate its self-assembly time during the film formation process. This could lead to a favorable vertical phase morphology with better molecular ordering of PM6 in the ternary system. Such favorable microstructure facilitated enhanced exciton dissociation, balanced charge transport, reduced trap density and energetic disorder, and mitigated energy loss. As a result, the optimized PM6:BTR-SCl:L8-BO blend delivered a champion PCE of 19.4% with simultaneously increased V_{OC} (0.89 V), J_{SC} (26.8 mA cm^{-2}), and FF (81.5%), much higher than the corresponding binary control based on PM6:L8-BO (PCE = 18.0%, V_{OC} = 0.88 V, J_{SC} = 26.2 mA cm^{-2}, FF = 78.1%). Moreover, the ternary devices also presented evidently extended photostability and thermal stability. Notably, the molecule BTR-SCl was introduced into the D18:L8-BO system, the D18:BTR-SCl:L8-BO based ternary device was even able to obtain an extraordinary PCE of 20.0% (V_{OC} = 0.92 V, J_{SC} = 26.9 mA cm^{-2}, FF = 80.9%). This work therefore offers a profound understanding of the morphological modulation process, especially for polymer assembly behaviors, which opens new avenues for further refining the multi-component techniques.

Author contributions

M. Z. conceived the idea. B. C. conducted device fabrication, carried out the corresponding characterization studies, and wrote the original draft. W. H. synthesized BTR-SCl and revised the manuscript. C. H. and S. C. helped analyze some experimental results and revise the manuscript. M. Z., X. G. and X. X. reviewed and edited the draft. X. G., Y. L., and M. Z. directed and supervised the project. All authors discussed the results and prepared the paper.

Data availability

The data that support the findings of this study are available from the corresponding author upon reasonable request.

Conflicts of interest

There are no conflicts of interest to declare.

Acknowledgements

This work was supported by the Shandong Provincial Natural Science Foundation (ZR2022JQ09), the Taishan Scholar Program at Shandong Province (tsqn202306061), the Collaborative Innovation Center of Suzhou Nano Science & Technology. The authors are grateful for the beam time and technical support provided by the in-house X-ray scattering beamline of the National Engineering Research Center for Colloidal Materials, Shandong University.

References

1 R. Søndergaard, M. Hösel, D. Angmo, T. T. Larsen-Olsen and F. C. Krebs, *Mater. Today*, 2012, **15**, 36–49.
2 Y. Li, X. Huang, H. K. M. Sheriff and S. R. Forrest, *Nat. Rev. Mater.*, 2023, **8**, 186–201.
3 X. Lu, C. Xie, Y. Liu, H. Zheng, K. Feng, Z. Xiong, W. Wei and Y. Zhou, *Nat. Energy*, 2024, **9**, 793–802.
4 O. P. Dimitriev, *Chem. Rev.*, 2022, **122**, 8487–8593.
5 S. Chandrabose, K. Chen, A. J. Barker, J. J. Sutton, S. K. K. Prasad, J. Zhu, J. Zhou, K. C. Gordon, Z. Xie, X. Zhan and J. M. Hodgkiss, *J. Am. Chem. Soc.*, 2019, **141**, 6922–6929.
6 J. Wang, Z. Zheng, P. Bi, Z. Chen, Y. Wang, X. Liu, S. Zhang, X. Hao, M. Zhang, Y. Li and J. Hou, *Natl. Sci. Rev.*, 2023, **10**, nwad085.
7 S. Guan, Y. Li, C. Xu, N. Yin, C. Xu, C. Wang, M. Wang, Y. Xu, Q. Chen, D. Wang, L. Zuo and H. Chen, *Adv. Mater.*, 2024, **36**, 2400342.
8 Y. Jiang, S. Sun, R. Xu, F. Liu, X. Miao, G. Ran, K. Liu, Y. Yi, W. Zhang and X. Zhu, *Nat. Energy*, 2024, **9**, 975–986.
9 L. Wang, C. Chen, Y. W. Fu, C. H. Guo, D. H. Li, J. C. Cheng, W. Sun, Z. R. Gan, Y. D. Sun, B. J. Zhou, C. H. Liu, D. Liu, W. Li and T. Wang, *Nat. Energy*, 2024, **9**, 208–211.
10 Y. Xu, H. Yao, L. Ma, J. Wang and J. Hou, *Rep. Prog. Phys.*, 2020, **83**, 082601.
11 K. Jiang, J. Zhang, C. Zhong, F. R. Lin, F. Qi, Q. Li, Z. Peng, W. Kaminsky, S.-H. Jang, J. Yu, X. Deng, H. Hu, D. Shen, F. Gao, H. Ade, M. Xiao, C. Zhang and A. K. Y. Jen, *Nat. Energy*, 2022, **7**, 1076–1086.
12 P. Li, J. Fang, Y. Wang, S. Manzhos, L. Cai, Z. Song, Y. Li, T. Song, X. Wang, X. Guo, M. Zhang, D. Ma and B. Sun, *Angew. Chem., Int. Ed.*, 2021, **60**, 15054–15062.
13 J. Yuan, C. Zhang, B. Qiu, W. Liu, S. K. So, M. Mainville, M. Leclerc, S. Shoaee, D. Neher and Y. Zou, *Energy Environ. Sci.*, 2022, **15**, 2806–2818.
14 Y. Jiang, Y. Li, F. Liu, W. Wang, W. Su, W. Liu, S. Liu, W. Zhang, J. Hou, S. Xu, Y. Yi and X. Zhu, *Nat. Commun.*, 2023, **14**, 5079.
15 M. Zhou, C. Liao, Y. Duan, X. Xu, L. Yu, R. Li and Q. Peng, *Adv. Mater.*, 2022, **35**, e2208279.
16 S. Gao, X. Li, R. Cao, X. Li, T. Chen, Y. Lu, J. Zhu and S. Yang, *ACS Energy Lett.*, 2024, **9**, 5037–5044.
17 K. Liu, Y. Jiang, G. Ran, F. Liu, W. Zhang and X. Zhu, *Joule*, 2024, **8**, 835–851.
18 M. Gao, J. Wu, X. Yuan, C. He, H. Jiang, W. Zhao, C. Duan, Y. Chen, Y. Ke, H. Yao and L. Ye, *Energy Environ. Sci.*, 2023, **16**, 5822–5831.
19 F. Sun, X. Wang, M. Wan, Z. Liu, Y. Luo, J. Ren, X. Zheng, T. Rath, C. Xiao, T. Hu, G. Trimmel and R. Yang, *Adv. Funct. Mater.*, 2023, **33**, 2306791.
20 L. Zhu, M. Zhang, J. Xu, C. Li, J. Yan, G. Zhou, W. Zhong, T. Hao, J. Song, X. Xue, Z. Zhou, R. Zeng, H. Zhu, C. C. Chen, R. C. I. MacKenzie, Y. Zou, J. Nelson, Y. Zhang, Y. Sun and F. Liu, *Nat. Mater.*, 2022, **21**, 656–663.
21 X. Guo, Q. Fan, J. Wu, G. Li, Z. Peng, W. Su, J. Lin, L. Hou, Y. Qin, H. Ade, L. Ye, M. Zhang and Y. Li, *Angew. Chem., Int. Ed.*, 2020, **60**, 2322–2329.
22 T. M. Clarke and J. R. Durrant, *Chem. Rev.*, 2010, **110**, 6736–6767.
23 H. Tian, W. Xu, Z. Liu, Y. Xie, W. Zhang, Y. Xu, S. Y. Jeong, F. Zhang, N. Weng, Z. Zhang, K. Wang, Q. Sun, J. Zhang, X. Li, X. Du, X. Hao, H. Y. Woo, X. Ma and F. Zhang, *Adv. Funct. Mater.*, 2024, **34**, 2313751.
24 Y. Wu, Q. Fan, B. Fan, F. Qi, Z. Wu, F. R. Lin, Y. Li, C.-S. Lee, H. Y. Woo, H.-L. Yip and A. K. Y. Jen, *ACS Energy Lett.*, 2022, **7**, 2196–2202.
25 L. Chen, J. Yi, R. Ma, T. A. Dela Peña, Y. Luo, Y. Wang, Y. Wu, Z. Zhang, H. Hu, M. Li, J. Wu, G. Zhang, H. Yan and G. Li, *Mater. Sci. Eng., R*, 2024, **159**, 100794.
26 K. Liu, Y. Jiang, F. Liu and X. Zhu, *Energy Environ. Sci.*, 2024, **17**, 4944–4967.
27 Y. Wei, Z. Chen, G. Lu, N. Yu, C. Li, J. Gao, X. Gu, X. Hao, G. Lu, Z. Tang, J. Zhang, Z. Wei, X. Zhang and H. Huang, *Adv. Mater.*, 2022, **34**, 2204718.
28 X. Cui, H. Li, H. Lu, Y. Liu, G. Ran, R. Liu, H. Zhang, X. Ma, D. Li, Y. Lin, J. Yu, W. Zhang, L. Cai, Y. Liu, P. Cheng, A. Zhang, Z. Ma, G. Lu and Z. Bo, *Sci. China: Chem.*, 2023, **67**, 890–897.
29 Y. Zhang, W. Deng, C. E. Petoukhoff, X. Xia, Y. Lang, H. Xia, H. Tang, H. T. Chandran, S. Mahadevan, K. Liu, P. W. K. Fong, Y. Luo, J. Wu, S.-W. Tsang, F. Laquai, H. Wu, X. Lu, Y. Yang and G. Li, *Joule*, 2024, **8**, 509–526.
30 J. Wang, M. Zhang, J. Lin, Z. Zheng, L. Zhu, P. Bi, H. Liang, X. Guo, J. Wu, Y. Wang, L. Yu, J. Li, J. Lv, X. Liu, F. Liu, J. Hou and Y. Li, *Energy Environ. Sci.*, 2022, **15**, 1585–1593.
31 Y. Liu, B. Liu, C.-Q. Ma, F. Huang, G. Feng, H. Chen, J. Hou, L. Yan, Q. Wei, Q. Luo, Q. Bao, W. Ma, W. Liu, W. Li, X. Wan, X. Hu, Y. Han, Y. Li, Y. Zhou, Y. Zou, Y. Chen, Y. Liu, L. Meng, Y. Li, Y. Chen, Z. Tang, Z. Hu, Z.-G. Zhang and Z. Bo, *Sci. China: Chem.*, 2022, **65**, 1457–1497.

32 H. Li, S. Liu, X. Wu, S. Yao, X. Hu and Y. Chen, *Energy Environ. Sci.*, 2023, **16**, 76–88.
33 G. Zhang, F. R. Lin, F. Qi, T. Heumüller, A. Distler, H.-J. Egelhaaf, N. Li, P. C. Y. Chow, C. J. Brabec, A. K. Y. Jen and H.-L. Yip, *Chem. Rev.*, 2022, **122**, 14180–14274.
34 X. Wan, C. Li, M. Zhang and Y. Chen, *Chem. Soc. Rev.*, 2020, **49**, 2828–2842.
35 C. Li, J. Zhou, J. Song, J. Xu, H. Zhang, X. Zhang, J. Guo, L. Zhu, D. Wei, G. Han, J. Min, Y. Zhang, Z. Xie, Y. Yi, H. Yan, F. Gao, F. Liu and Y. Sun, *Nat. Energy*, 2021, **6**, 605–613.
36 H. Bai, Q. Fan, R. Ma, X. Guo, W. Ma and M. Zhang, *Chin. J. Chem.*, 2024, **42**, 1307–1318.
37 H. Bin, S. Gao, X. Wang, F. Cao, Y. Chen, J. Zhang, L. Bu, X. Song and G. Lu, *Energy Environ. Sci.*, 2024, **17**, 7803–7815.
38 L. Zhang, L. Hu, X. Wang, H. Mao, L. Zeng, L. Tan, X. Zhuang and Y. Chen, *Adv. Funct. Mater.*, 2022, **32**, 2202103.
39 Q. Liu, Y. Wang, J. Fang, H. Liu, L. Zhu, X. Guo, M. Gao, Z. Tang, L. Ye, F. Liu, M. Zhang and Y. Li, *Nano Energy*, 2021, **85**, 105963.
40 J. Li, C. Zhang, X. Sun, H. Wang, H. Hu, K. Wang and M. Xiao, *Nano Energy*, 2024, **125**, 109542.
41 Q. Xie, X. Deng, C. Zhao, J. Fang, D. Xia, Y. Zhang, F. Ding, J. Wang, M. Li, Z. Zhang, C. Xiao, X. Liao, L. Jiang, B. Huang, R. Dai and W. Li, *Angew. Chem., Int. Ed.*, 2024, **63**, e202403015.
42 H. Liang, Y. Wang, X. Guo, D. Yang, X. Xia, J. Wang, L. Zhang, Y. Shi, X. Lu and M. Zhang, *J. Mater. Chem. A*, 2022, **10**, 10926–10934.
43 C. Sun, J.-W. Lee, C. Lee, D. Lee, S. Cho, S.-K. Kwon, B. J. Kim and Y.-H. Kim, *Joule*, 2023, **7**, 416–430.
44 P. Wang, J. Zhang, D. Luo, J. Xue, L. Zhang, H. Mao, Y. Wang, C. Yu, W. Ma and Y. Chen, *Adv. Funct. Mater.*, 2024, **34**, 2402680.
45 N. Gasparini, X. Jiao, T. Heumueller, D. Baran, G. J. Matt, S. Fladischer, E. Spiecker, H. Ade, C. J. Brabec and T. Ameri, *Nat. Energy*, 2016, **1**, 16118.
46 C. Cao, H. Wang, D. Qiu, T. Zhao, Y. Zhu, X. Lai, M. Pu, Y. Li, H. Li, H. Chen and F. He, *Adv. Funct. Mater.*, 2022, **32**, 2201828.
47 X.-K. Chen, D. Qian, Y. Wang, T. Kirchartz, W. Tress, H. Yao, J. Yuan, M. Hülsbeck, M. Zhang, Y. Zou, Y. Sun, Y. Li, J. Hou, O. Inganäs, V. Coropceanu, J.-L. Bredas and F. Gao, *Nat. Energy*, 2021, **6**, 799–806.
48 C. Zhang, J. Yuan, J. K. W. Ho, J. Song, H. Zhong, Y. Xiao, W. Liu, X. Lu, Y. Zou and S. K. So, *Adv. Funct. Mater.*, 2021, **31**, 2101627.
49 F. Zhao, D. He, C. Zou, Y. Li, K. Wang, J. Zhang, S. Yang, Y. Tu, C. Wang and Y. Lin, *Adv. Mater.*, 2023, **35**, e2210463.
50 Z. Chen, H. Yao, J. Wang, J. Zhang, T. Zhang, Z. Li, J. Qiao, S. Xiu, X. Hao and J. Hou, *Energy Environ. Sci.*, 2023, **16**, 2637–2645.
51 J. A. Carr and S. Chaudhary, *Energy Environ. Sci.*, 2013, **6**, 3414–3438.
52 Z. Chen, J. Zhu, D. Yang, W. Song, J. Shi, J. Ge, Y. Guo, X. Tong, F. Chen and Z. Ge, *Energy Environ. Sci.*, 2023, **16**, 3119–3127.
53 Y. Cheng, B. Huang, X. Huang, L. Zhang, S. Kim, Q. Xie, C. Liu, T. Heumüller, Z. Liu, Y. Zhang, F. Wu, C. Yang, C. J. Brabec, Y. Chen and L. Chen, *Angew. Chem., Int. Ed.*, 2022, **61**, e202200329.
54 J. Zhang, H. Mao, K. Zhou, L. Zhang, D. Luo, P. Wang, L. Ye and Y. Chen, *Adv. Mater.*, 2024, **36**, 2309379.
55 F.-Z. Cui, Z.-H. Chen, J.-W. Qiao, T. Wang, G.-H. Lu, H. Yin and X.-T. Hao, *Adv. Funct. Mater.*, 2022, **32**, 2200478.
56 Y. Wang, S. Zhang, J. Wang, J. Ren, J. Qiao, Z. Chen, Y. Yu, X.-T. Hao and J. Hou, *ACS Energy Lett.*, 2024, **9**, 2420–2427.

